XX Polish Fluid Mechanics Conference,
Gliwice, 17-20 September 2012

VORTEX WAKE PATTERNS IN FLOW OVER A OSCILLATING PROFILE

Tomasz Kozłowski[1], Henryk Kudela[1],
[1]*Institute of Aerospace, Process and Power Machines Engineering,*
Wroclaw University of Technology, 50-370 Wroclaw, Wybrzeze Wyspianskiego 27, Poland
E-mail: henryk.kudela@pwr.wroc.pl, tomasz.kozlowski@pwr.wroc.pl

Abstract
Fish, birds and insects, flap their wings or fins to an extremely effective movement in surrounding fluid. It's well known that the hydrodynamic forces generation in the flapping motion is ruled by the unsteady fluid phenomena. In the paper we presented the unsteady effects that led to the vertical and thrust force production by the foil which was in simply harmonic (plunging) motion and was immerse in uniform stream of fluid. Vortex-In-Cell method was used to investigate the hydrodynamic effects Inversion of the vortices topology in the vortex Karman street results in propulsion force production. By setting the proper parameters of oscillations, the asymmetry in the foil wake appeared with results in generation of the lift and thrust force. The relationship between Strouhal number, amplitude of oscillations and vortices topology behind the foil for different Reynolds numbers was established numerically. With the increasing of the Reynolds number we observe the bursting of boundary layer from the profile and reduction of the lift force.

Key words: Vortex in cell, flapping motion, vortex wake

INTRODUCTION

The great interests in the low Reynolds number unsteady aerodynamics stems from the increasing importance in the micro air vehicles and from the will to understand the aerodynamics of natural flyers. Flapping motion is a basic mode of locomotion in birds, insects and fishes. The basic question birds and insects flight is how do they generate enough lift and the thrust force to be able to perform remarkable maneuvers with rapid accelerations and decelerations. From the point of the fluid mechanics we believe that all the phenomena that are related to the generation of hydrodynamic forces are ruled by the dynamics of the vorticity. Especially the behavior of the boundary layer creation, its separation from the solid boundary are extremely important. The Karman vortex street in the flow over the profile generate the drag force. On the other side, the oscillating profile may reverse Karman vortex street producing the thrust force. Although flight in nature is naturally three-dimensional, when the ratio of the span to the chord is large enough, the two-dimensional model is widely used (Peskin and Miller, 2004), (Wang, 2004), (Wang et al., 2000), (Sane, 2003). The primary parameters that characterize the oscillation of the foil and fluid motion, was the Strouhal number (St_A), the Reynolds number (Re) and the amplitude of oscillation (A_0). We demonstrated dependence between those numbers and vortex wake topology. In the range of proper combination of oscillation we observed the reverse vortex Karman street and deflection of this street from the main direction of the flow. For numerical study we choose the Vortex-In-Cell (VIC) method. The importance of the vortex

particle method lies in the possibility of the analyzing more easily and directly the vorticity field due to fact that in computation the vortex particles that carry the information about the vorticity field are used. Attractive feature of the method is also the elimination of pressure from equation of the fluid motion.
The vortex wake and its influence on thrust production by the oscillating foil has been the subject of wide interests (Anderson et al., 1998), (Godoy-Diana et al., 2009), (Jones et al., 1996).

THE VORTEX-IN-CELL METHOD

Governing equations in non-inertial reference frame

The Navier-Stokes equation in primitive variables with the coordinates fixed to the moving body has the form (Wang, 2004)

$$\frac{\partial \mathbf{u}}{\partial t} + \nabla \mathbf{u} \cdot \mathbf{u} = -\nabla p + \nu \Delta \mathbf{u} - \frac{d\mathbf{U_0}}{dt} - \tag{1}$$
$$\frac{d\mathbf{\Omega_0}}{dt} \times \mathbf{r} + 2\mathbf{\Omega_0} \times \mathbf{u} + \mathbf{\Omega_0} \times (\mathbf{\Omega_0} \times \mathbf{r}),$$
$$\nabla \cdot \mathbf{u} = 0, \tag{2}$$

where $\mathbf{\Omega_0}$ is the angular and $\mathbf{U_0}$ is the translation velocity vector of the profile. The last three terms in equation (1) arise from non-inertial coordinate system and denote non-inertial force due to rotational acceleration, the Coriolis force and the centrifugal force respectively. Taking the curl by the both side of the equation (1), it can be transform to the form (Gustafson et al., 1991)

$$\frac{\partial(\omega + 2\Omega_0)}{\partial t} + (\nabla \omega) \cdot \mathbf{u} = \nu \Delta \omega, \tag{3}$$
$$\Delta \psi = -\omega, \tag{4}$$
$$\mathbf{u} = \nabla \times (0, 0, \psi). \tag{5}$$

The equation (3) and (4) represent the vorticity transport equation in moving non-inertial reference frame (for observer moving with the body). The stream function far from the body due to translational velocity U_0, and the angular rotation $\Omega_0 = \frac{d\alpha}{dt}$, can be write as

$$\psi_\infty = U_0(y\cos(\alpha) - x\sin(\alpha)) - \frac{\Omega_0}{2}(x^2 + y^2). \tag{6}$$

The vorticity field observed in the laboratory frame, differs only by a constant from the vorticity in the non-inertial frame therefore, we introduce the following change of variables

$$\omega^* = \omega + 2\Omega_0 \quad \text{and} \quad \psi^* = \psi - \psi_\infty. \tag{7}$$

The detailed description of solution of the Helmholtz equations in moving reference frame can be found in (Gustafson et al., 1991).

Vortex-In-Cell method for conformal geometry

In order to better fit of numerical grid to solid boundary and to have the possibility of using fast elliptic solver, we transform non-rectangular physical region x, y – variables to the rectangular one (ξ, η). The following conformal transformation was applied

$$x + iy = \cosh(\xi + i\eta). \tag{8}$$

In new variables (ξ, η), taking into account (7), the equations (3), (4) have the form

$$\frac{\partial \omega}{\partial t} + (\nabla \omega) \cdot \mathbf{u} = \frac{\nu}{J} \Delta \omega, \tag{9}$$
$$\Delta \Psi = -J\omega, \tag{10}$$

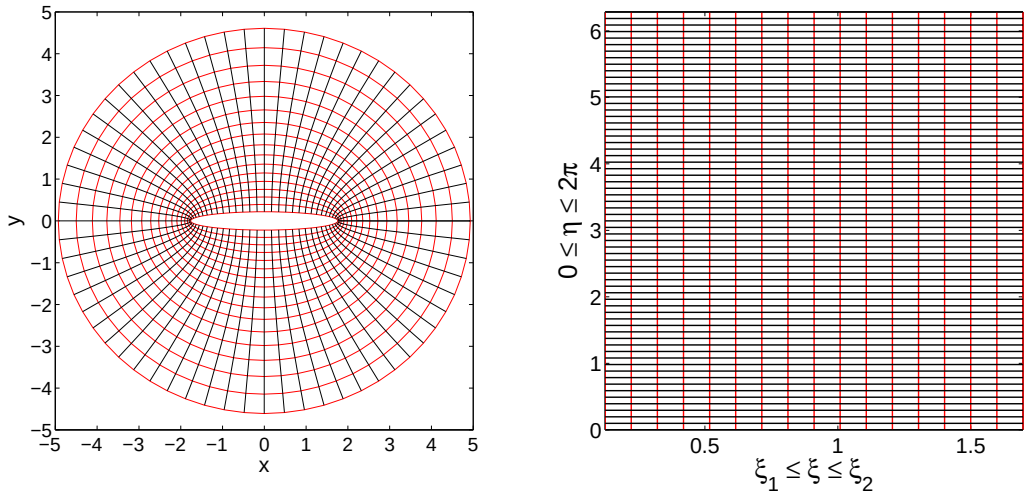

Fig. 1. *Elliptical and rectangular grid in the physical domain and the transform domain.*

where J denotes Jacobian of the conformal transformation

$$J = \det \begin{vmatrix} x_\xi & x_\eta \\ y_\xi & y_\eta \end{vmatrix}. \tag{11}$$

We have already omitted the star index. The velocity field $\mathbf{u}(u, v)$ is expressed by the formulas

$$u = \frac{1}{J}\frac{\partial \psi}{\partial \eta}, \quad v = -\frac{1}{J}\frac{\partial \psi}{\partial \xi}. \tag{12}$$

The nullifying of the normal velocity component is obtained by setting $\psi =$ const. on the wall. The no-slip condition is realized by introducing a proper portion of vorticity, that ensure the condition $\mathbf{u} \cdot \mathbf{s}^0 = 0$ were $\mathbf{s}^0$ is tangential unit vector (Koumoutsakos et al., 1994), (Weinan and Liu, 1996).

In the VIC method the continuous vorticity field is approximated with the discrete particles distribution. The flow region is covered with the numerical grid $h = \Delta\eta = \Delta\xi$. In every grid node, the particles with circulation $\Gamma_j = \int_A \omega d\xi d\eta$ are placed, where $A = h^2$, and

$$\omega(\xi, \eta) = \sum_p \Gamma_p \delta(\xi - \xi_p)\delta(\eta - \eta_p). \tag{13}$$

The viscous splitting algorithm (Cottet and Koumoutsakos, 2000) was used for solution of (9), (10). At first step, the inviscid fluid motion equation was solved

$$\frac{\partial \omega}{\partial t} + (\nabla \omega) \cdot \mathbf{u} = 0. \tag{14}$$

From (14) stems that vorticity is constant along the trajectory of the fluid particles. According to Helmholtz theorem (Wu et al., 2005), vortex particles move like material fluid particles. The differential equation (14) is replaced by the set of ordinary equations

$$\frac{d\xi}{dt} = u, \quad \frac{d\eta}{dt} = v, \quad \xi(0, \alpha_1) = \alpha_1, \quad \eta(0, \alpha_2) = \alpha_2, \tag{15}$$

where $\alpha = (\alpha_1, \alpha_2)$ means Lagrangian coordinate of fluid particles. The number of the particles are equal to the number of the grid nodes. The Lagrangian parameter α takes in each time step the value $\alpha_i, \alpha_j = (\xi_i, \eta_j)$. The finite set of equations (15) was solved by fourth order Runge-Kutta method. The velocity field was obtained by solving Poisson equation (10) on the

numerical grid and utilizing (12). The velocities of the particles that are found between the grid nodes were calculated by the interpolation formula

$$u(\xi_p, \eta_p) = \sum_j l_j(\xi_p, \eta_p) u_j, \tag{16}$$

where l_j denotes two dimensional bilinear interpolation Lagrange base.

At second step the viscosity was taken into account and the diffusion equation was solved

$$\frac{\partial \omega}{\partial t} = \frac{\nu}{J} \Delta \omega, \tag{17}$$

$$\omega(\xi, \eta, 0) = \omega_0, \quad \omega|_{wall} = \omega_s, \tag{18}$$

where ω_s was calculated on the basis of the Poisson equation (10). The non–slip condition $u = 0$, gives the vorticity on the wall $\omega_{(0,j)_s} = -\psi_{\eta\eta}/J$. The value of $\psi_{\eta\eta}$ was calculated from the Briley formula (Weinan and Liu, 1996)

$$\omega_{(0,j)_s} = \frac{1}{J} \frac{108\psi_{1,j} - 27\psi_{2,j} + 4\psi_{3,j}}{18h^2} + O(h^4), \tag{19}$$

where h denotes the grid step, index 0 refers to the wall and index $i,\ i = 1, 2, 3$ to the distance ih from the wall.

After particles displacement according to the ordinary differential equations (15), one have to transfer the vorticity from the particles to the grid nodes using the interpolation, Fig. 2. It was done, according to the formula

$$\omega_{ij} = \frac{1}{h^2} \sum_p \Gamma_p \varphi_h(\xi) \varphi_h(\eta), \tag{20}$$

where

$$\varphi_h(\xi) = \varphi\left(\frac{\xi - \xi_i}{h}\right), \quad \varphi_h(\eta) = \varphi\left(\frac{\eta - \eta_j}{h}\right). \tag{21}$$

Indexes p, i, j refer to the vortex particles and grid nodes respectively and $\varphi(\cdot)$ denote the kernel of the interpolation function. Interpolation of particle masses onto the grid nodes has the fundamental meaning for the precision of the VIC method. In present work the redistribution process was performed using Z-splines (Sagredo, 2003). The main advantage of these formulas is easy construction of high order symmetrical functions and also one-sided interpolation function to apply near the boundary. Four order interpolation kernel Z_2 is identical with known in literature $M4$ kernel, and has the form (Sagredo, 2003), (Koumoutsakos and Leonard, 1995)

$$\varphi(x) = \begin{cases} 1 - \frac{5}{2}x^2 + \frac{3}{2}|x|^3 & \text{for } |x| < 1 \\ \frac{1}{2}(2 - |x|)^2(1 - |x|) & \text{for } 1 \le |x| \le 2. \\ 0 & \text{for } |x| > 2 \end{cases} \tag{22}$$

For particles near the wall one-sided interpolation functions were used, derived according to the algorithm presented in (Sagredo, 2003) (see fig. 2 on the right)

$$\varphi(x) = \begin{cases} 1 + \frac{1}{2}x^2 - \frac{3}{2}|x| & \text{for } j = 0, |x| \le 1 \\ -x^2 + 2|x| & \text{for } j = 1, |x| \le 1. \\ \frac{1}{2}x^2 - \frac{1}{2}|x| & \text{for } j = 2, |x| \le 1 \end{cases} \tag{23}$$

Both interpolation kernels conserve three first moments (Cottet and Koumoutsakos, 2000)

$$\sum_p x_p^\alpha \varphi\left(\frac{x_p - x}{h}\right) = x^\alpha, \qquad \alpha = 0, 1, 2. \tag{24}$$

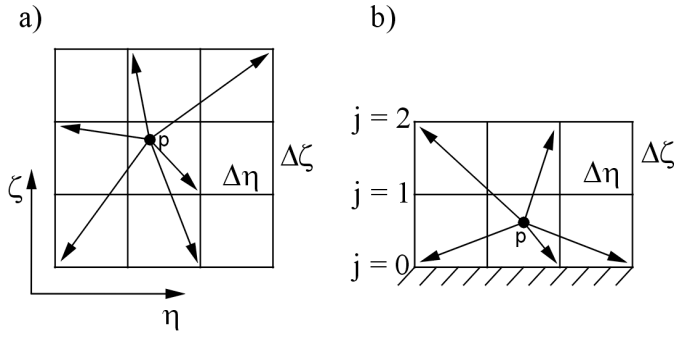

Fig. 2. *Redistribution of the particle masses onto the neighboring grid nodes, a) for particles laying inside of the computational domain (at least one cell from the wall), b) for the particles in the vicinity of the wall.*

After redistribution the diffusion equation (17) was solved on the numerical grid with alternating direction implicit (ADI) scheme (Thomas, 1995)

$$\omega^{n+\frac{1}{2}} = \omega^n + \frac{\Delta t}{2J}\nu\left(\Lambda_{\xi\xi}\omega^n + \Lambda_{\eta\eta}\omega^{n+\frac{1}{2}}\right), \tag{25}$$

$$\omega^{n+1} = \omega^{n+\frac{1}{2}} + \frac{\Delta t}{2J}\nu\left(\Lambda_{\xi\xi}\omega^{n+1} + \Lambda_{\eta\eta}\omega^{n+\frac{1}{2}}\right). \tag{26}$$

where Λ means of the three point central finite difference quotient, with respect to the variable that was put in lower index. The solution of the diffusion equation ends the calculations in the n-th time step of the Vortex-In-Cell method. The VIC method was very carefully tested and results were published in several our papers (Kudela and Kozlowski, 2009), (Kudela and Malecha, 2009).

Unbounded domain

Due to fact that we use the numerical grid, the domain of computation have to be finite. To establish of the boundary condition for stream function far from the body, we used the method described in (Anderson and Reider, 1996), (Wang, 1999). That method takes advantage of the fact that the domain of non–zero vorticity around the solid body is limited to the domain around the obstacle. In the far distance from the body where the vorticity is zero the asymptotic properties of the solution of Laplace equation and its representation by Fourier series is used. The detailed description of the obtaining the correct boundary value, applied in present work can be found in (Kudela and Kozlowski, 2009).

Hydrodynamic forces acting on the body

The hydrodynamic forces acting on the profile, were calculated using the vorticity distribution on the surface of the ellipse

$$\mathbf{F}_p = \nu\rho b\int_A \frac{\partial\omega}{\partial\mathbf{n}}dA + \rho A_b\frac{d\mathbf{U}_0}{dt}, \tag{27}$$

$$\mathbf{F}_\nu = \nu\rho b\int_A \omega\mathbf{s^0}dA, \tag{28}$$

where ρ denote density of the fluid, $\mathbf{n}$ and $\mathbf{s}^0$ is normal and tangential unit vector respectively, A_b is the area of the body and b is the contractual length normal to the plane of flow. The last term on the right side in equation (27) represent the inertial force of the fluid displaced by the profile (Sane, 2003). The forces obtained from equations (27), (28) were decomposed on to horizontal F_D and vertical F_L components, that correspond to the drag and lift forces. The forces coefficients were calculated according to relations

$$C_D = F_D/\frac{\rho}{2}U_0^2cb, \qquad C_L = F_L/\frac{\rho}{2}U_0^2cb, \tag{29}$$

where U_0 denotes the freestream translational velocity.

SIMULATION OF THE FLOW OVER OSCILLATING FOIL

Formulation of the problem and computation details

The main subject of our study is elliptic profile with prescribed motion according to the equation

$$y(t) = \frac{A_0}{2}\cos(2\pi f t), \tag{30}$$

where $y(t)$ denotes instantaneous position of the profile center, A_0 is the amplitude and f is the frequency of the oscillation. The airfoil vertical velocity is calculated from the formula $v = \frac{dy}{dt}$. Far from the body we assumed that velocity of the fluid U_0 is constant, Fig. 3. In literature, a motion described by the equation (30) is known as a plunging.

The flow over oscillating foil can be characterized by the Reynolds number $Re = \frac{U_0 c}{\nu}$, where c is the chord of the foil and ν is a kinematic coefficient of fluid viscosity, Strouhal number $(St = \frac{fc}{U_0})$, where c means chord length, and dimensionless amplitude of oscillation $A_c = \frac{A_0}{c}$ (Godoy-Diana et al., 2009), (Shyy et al., 2008).

The chord was set to $c = 2$ and thickness of the profile $e = 0.4$. We perform the calculations for the constant Reynolds number $Re = 100$ and homogeneous fluid with density $\rho = 1$. The plunging frequency was fixed to $f = 0.5$ and the Strouhal number (St) was controlled by changing of the free stream velocity U_0. The calculations were carried on for dimensionless time $t = fT$, in range $T = (0, 10)$ which correspond to ten period in the equation (30).

To resolve the flow, we use the elliptical mesh, given in Fig. 1, with 256 grid nodes in radial direction and 256 grid nodes in azimuthal direction. In every time step, we perform the correction of the boundary condition for the stream function far from the body, as detailed in previous section.

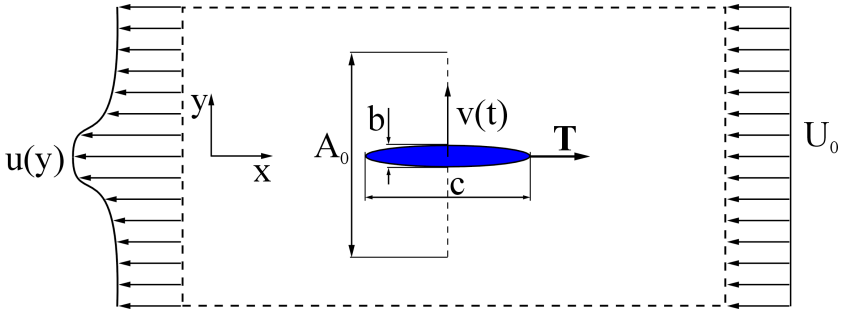

Fig. 3. *Scheme of the plunging airfoil immersed in the fluid.*

Vortex wakes for oscillating motion with $Re = 100$

It's well known, that the hydrodynamic forces exerted on the body immersed in the fluid can be explain by the dynamics of vorticity (Wu, 1981), (Wu et al., 2005). In Fig. 4÷8 the various vortex wake behind the flapping foil is presented after ten period of oscillation of the profile. For given Reynolds number $Re = 100$ and for the small amplitude of oscillations we observed a typical steady bubbles behind the profile. If the amplitude of oscillation increase the vortex bubbles loss its stationary character forming Karman vortex street, Fig. 4. The vortices shed from the upper (lower) side of the profile stay on the upper (lower) side of axis of symmetry. Such kind of vortex topology reduces fluid momentum in the wake cause the drug production. On the left side of the Fig. 4 the vortex street was visualized by the streak lines that were created by passive particles taken by fluid from surface of the profile. On the right side of the figures the flow is visualized by vorticity and streamlines. In Fig. 5 ($St = 0.8$, $A_C = 0.5$) we presented the vortex path that is called align vortices (av). It means that the vortices take place on the axis of symmetry.

The oscillating profile form dipolar structures which are convected downstream. Inversion of the topology of the vortices raised that led to the production of thrust force. The counter-

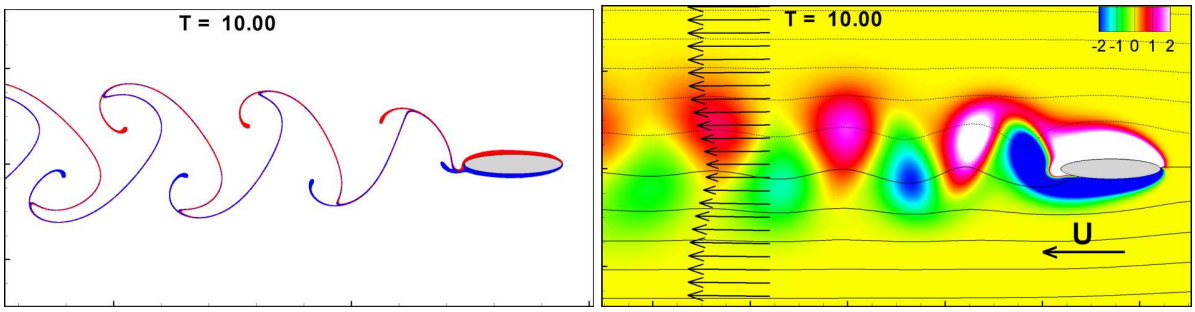

Fig. 4. *Karman vortex street produced by flapping flight with* $St = 0.6$ *and* $A_c = 0.25$. *On the top visualisation by passive markers is presented, on the bottom vorticity field with streamlines. The arrows behind the airfoil denotes averaged fluid velocity profile. The arrow on the bottom right correspond to value of the freestream velocity* U. *Denoted with* ⋆ *in Fig. 9.*

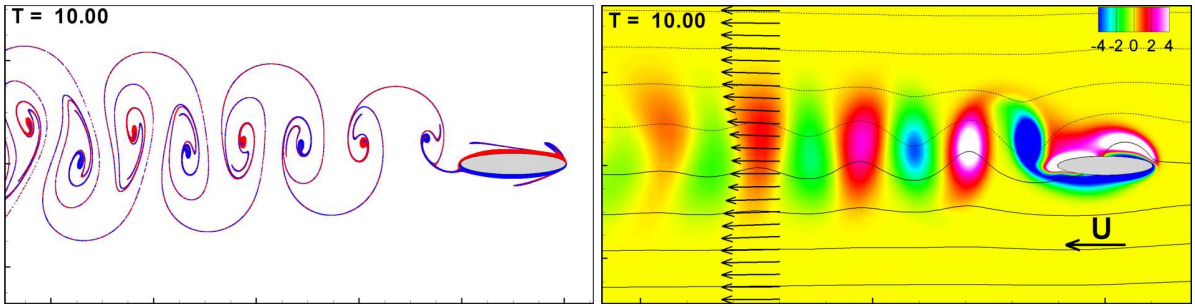

Fig. 5. *Aligned vortices generated by flapping flight with* $St = 0.8$ *and* $A_c = 0.5$. *The vortex wake correspond to transient region, in Fig. 9, denoted with* ▲.

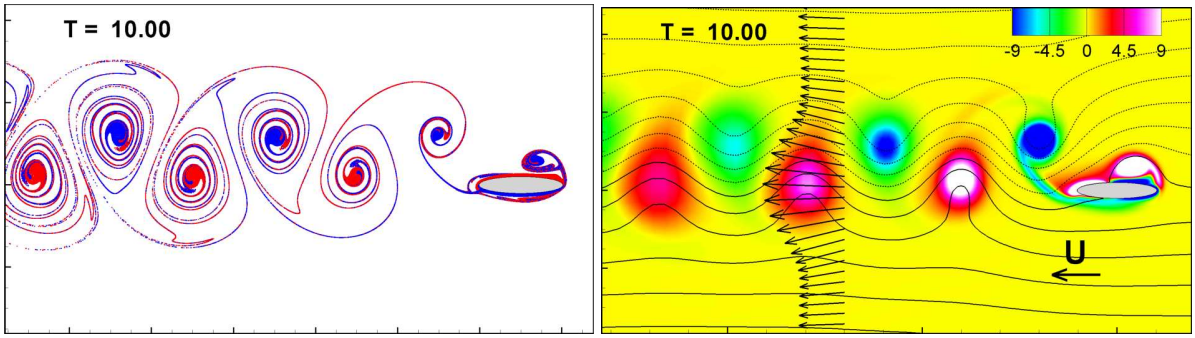

Fig. 6. *Thrust production by the plunging profile with* $St = 0.8$ *and* $A_c = 0.75$. *The reversed Karman vortex street denoted with* ● *in Fig. 9.*

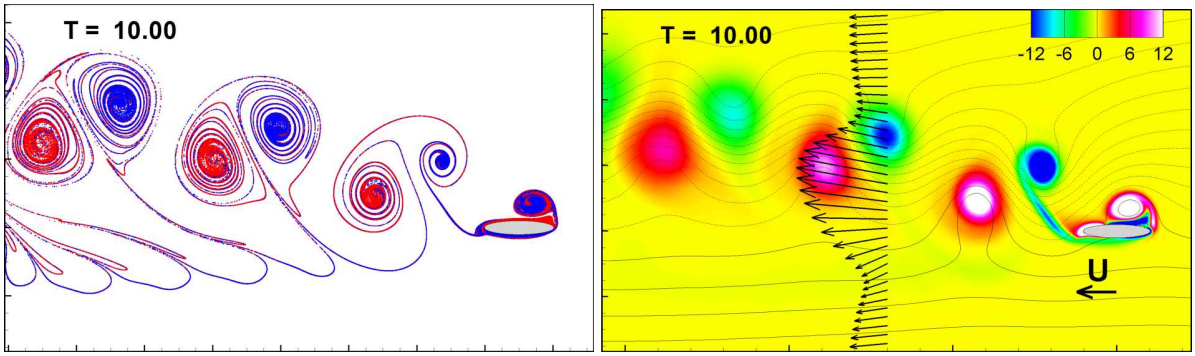

Fig. 7. *Deflected wing wake behind the plunging profile with* $St = 0.8$ *and* $A_c = 1.0$. *The upward deflection of the wink wake results in lift production, denoted in Fig. 9 with* ■.

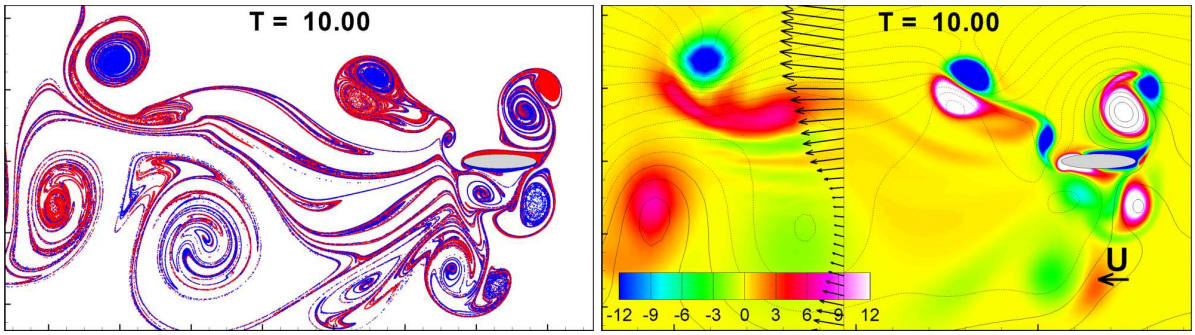

Fig. 8. *Random vorticity field generated by plunging foil with high value of Strouhal number* $St = 1.2$ *and amplitude* $A_c = 1.0$*. The presented case correspond to region denoted with* ♦ *in Fig. 9.*

rotating vortices in the wake increase the fluid momentum forming jet flow, Fig. 6. The vortices sheded on the upper surface of the profile change the position and pass to the below of symmetry axis. The vortices created on the lower part of the profile surface pass to the upper positions. Further increase the oscillating amplitude ($St = 0.8$, $A_C = 1.0$) leads to the the asymmetry of the wake and the deflection of the reverse Karman vortex street from horizontal direction Fig. 7. We abbreviated that structure by "drvKs" on the figure 8. Deflection on the wake led to generation of the the lift force (Jones et al., 1996), (Platzer and Jones, 2000). What is unexpected, the direction of the wake deflection depends on direction of the first flap, up or down and determines the direction of the horizontal acting force. Although the discussed phenomena was first observed by in the 50-s, the full explanation is still not complete (Godoy-Diana et al., 2009), (Godoy-Diana et al., 2008). Further increase of the Strouhal number or amplitude of oscillations results in loss in regular arrangement of vortices (see Fig. 8). The random distribution of vorticity cause random forces that act on the profile.

One can summarized the above results in phase space diagrams. In Fig. 9 the relation between the wake type and Strouhal number St and amplitude of oscillation is presented. The drag and lift coefficient are also depicted. the reversion of the topology of the vortex in the wake did not lead immediately to the thrust force generation. Only over the curve $C_D = 0$, the thrust force arise. It is consistent with experimental observations (Godoy-Diana et al., 2008). The positive lift force appears for whole region with deflected and reversed Karman vortex street. As for the thrust force, the positive lift force appear over the curve $C_L = 0$. The similar the phase space diagram for (St, A_C) was obtained experimentally for pitching profile (Godoy-Diana et al., 2008), (Godoy-Diana et al., 2009). The experimental data shown in cited papers are related with the foil that is subjected to the motion with varying angle of attack, called in the literature as a pitching. Despite the fact the Reynolds number was different (we assume $Re = 100$ and in cited work $Re = 1173$), the qualitative agreement of the following calculations with the discussed experimental data may suggest, that in given Reynolds number regime the mechanism of generation the thrust and the lift force are comparable.

Effect of the Reynolds number

Based on the numerical calculations we construct the phase transitions diagrams for Reynolds number $Re = 250$ and $Re = 500$. In this regime we observe another type of vortex wake which is called as **2P** vortex wake, recognized for the problem of flow around an oscillating cylinder (Ponta and Aref, 2006) and also for the flapping foil as noticed in (Schnipper et al., 2009). The **2P** means that in every foil oscillation two vortex pairs consisted with vortices of the opposite circulation are created, Fig. 10. By the experimental investigations reported in (Müller et al., 2008), it was found, that this type of vortex wake may be important in locomotion of the swimming fishes. The phase diagrams for the Reynolds number $Re = 250$ and $Re = 500$ are presented in Fig. 11a and 11b. What was unexpected, the region with reversed and deflected vortex wake (denoted with dings) for nondimensional time $T = 10$ become narrower

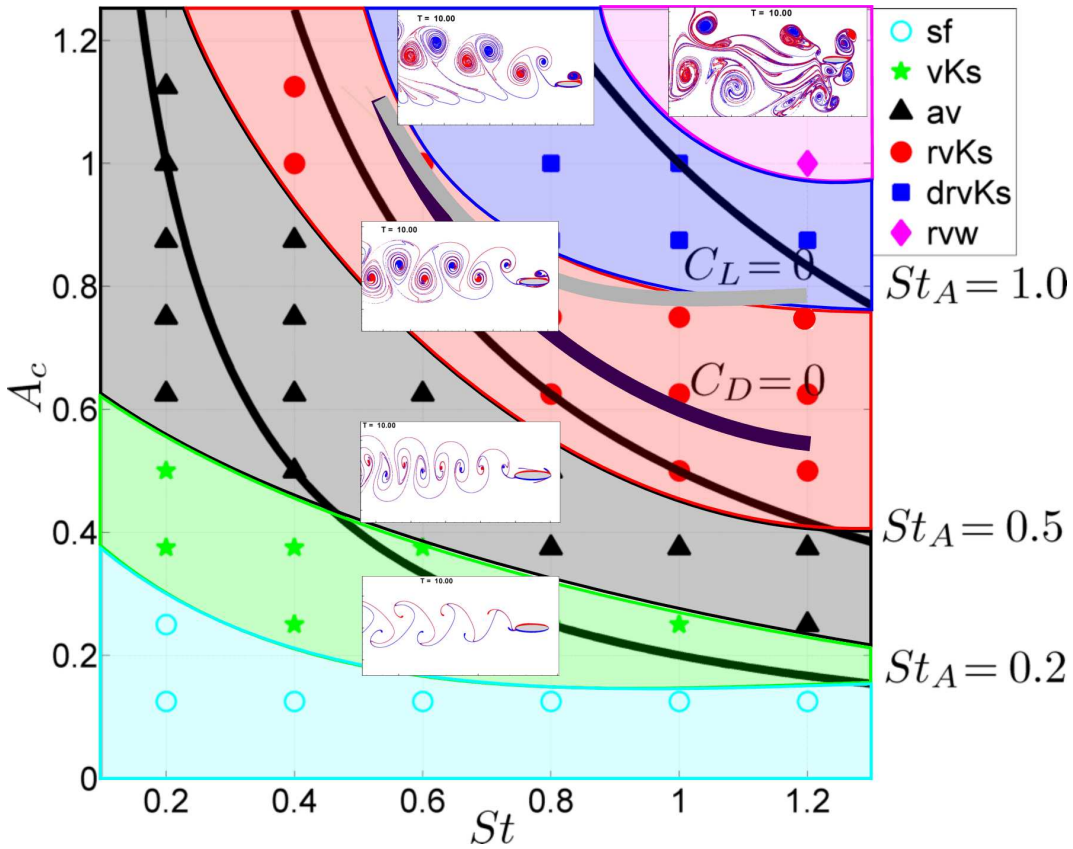

Fig. 9. *Relationship between Strouhal number St, nondimensional flapping amplitude A_c and vortex topology in the wing wake, from present computation for Reynolds number $Re = 100$. Symbols denotes: ○ - steady flow, ⋆ - Karman vortex street, ▲ - aligned vortices, ● - reversed Karman vortex street, ■ - deflected reversed Karman vortex street, ♦ - chaotic vortex wake.*

as Reynolds number increase and for the Reynolds number $Re = 500$ disappear at all. For Reynolds number $Re = 100$, the transition process proceed from the reversed Karman vortex street to chaotic vorticity field directly (see Fig. 11b). It means that production of the vertical force connected with the deflection of the vortex wake is not possible in this regime of parameters. We perform additional calculation near the transition line and after ten period of oscillation we don't observe the deflection of the vortex wake. However, at the start of the motion the deflection exist but after few foil oscillations we observe the straightening of the vortex wake, Fig. 12. In the investigated range of parameters the hydrodynamic effects generated by an oscillating profile are dominated by the phenomena of sudden separation and detachment of the boundary layer from the profile. If the intensity of the leading edge vortex is sufficiently high, it induces the vortex structure on the wall with opposite circulation, Fig. 13, frame for $T = 6.55$. This leads to the boundary layer separation (Fig. 13, $T = 7.20$), called the eruption of the boundary

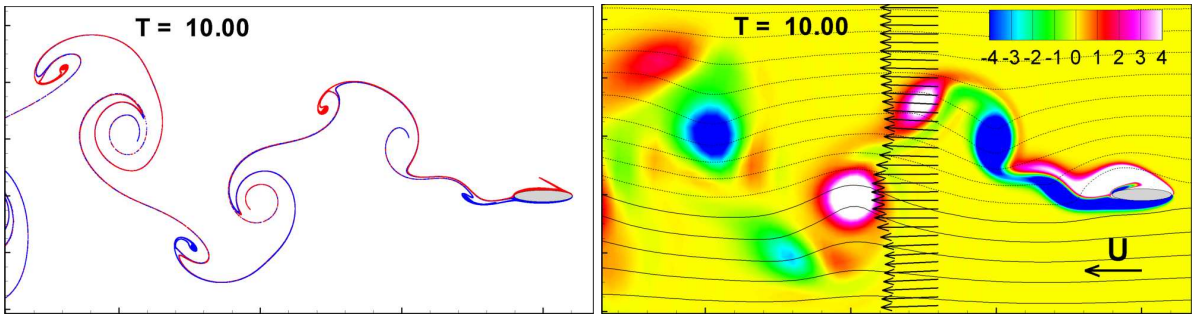

Fig. 10. *2P vortex wake, generated by plunging foil with Strouhal number $St = 0.2$, amplitude $A_C = 1.0$ and Reynolds number $Re = 250$. The presented case correspond to region denoted with ▼ in Fig. 11.*

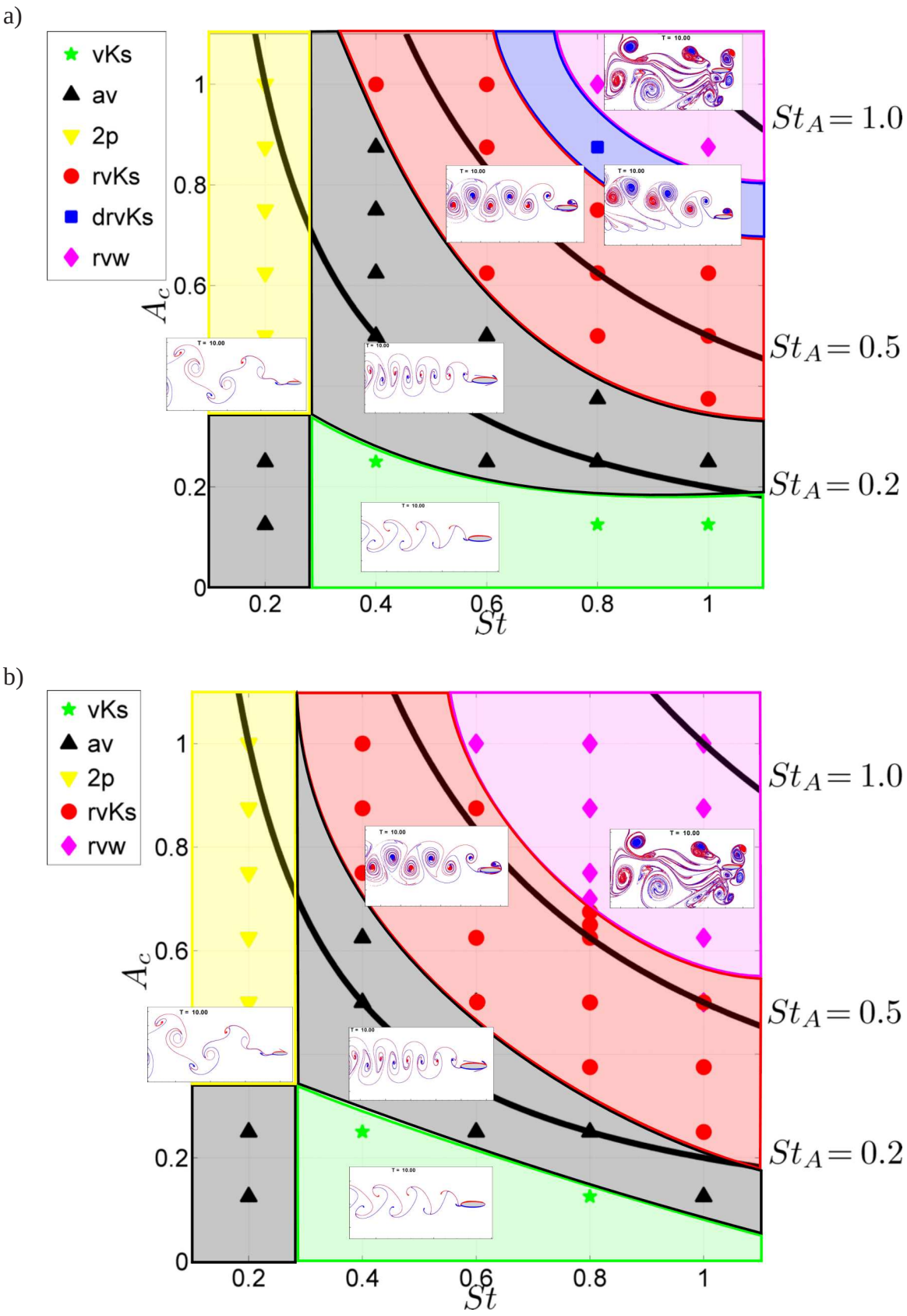

Fig. 11. Relationship between Strouhal number St, nondimensional flapping amplitude A_c and vortex topology in the wing wake, a) $Re = 250$ and b) $Re = 500$. Symbols in figure denotes: ▼ - **2P** vortex wake, ⋆ - Karman vortex street, ▲ - aligned vortices, ● - reversed Karman vortex street, ■ - deflected reversed Karman vortex street, ♦ - chaotic vortex wake.

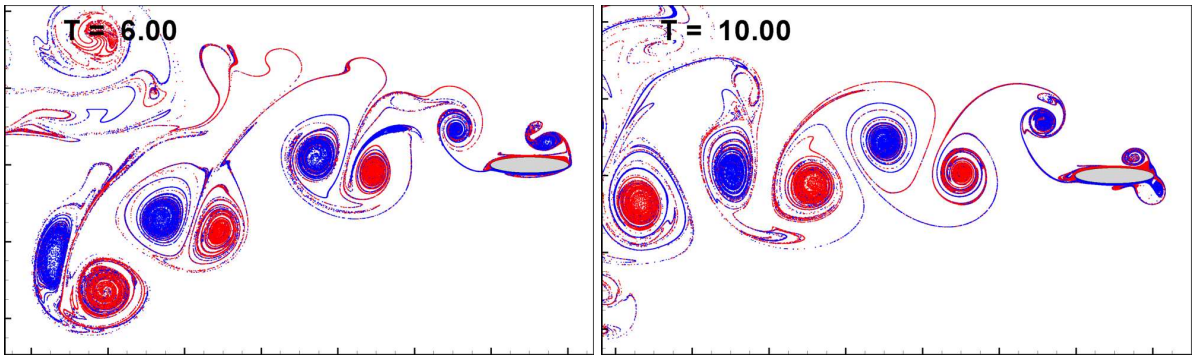

Fig. 12. *Effect of straightening of the vortex wake, caused by the dynamic eruption of the boundary layer,* $St = 0.8$, $A_C = 0.675$, $Re = 500$.

layer. The detailed description of the presented flow phenomena can be found in (Kudela and Malecha, 2010). The dynamics of the described eruption phenomena, causes in change of the vortex wake type, and loss of the deflection of the vortex wake. The boundary layer separation feed the flow area with the dipole vortex structures which eliminate the deflection of the vortex wake. It's seems that deflection of the vortex wake is very sensitive to the phenomena that is generated in the close vicinity of the profile. We believe that the primary cause of the loss of deflection of the vortex paths is connected with the non-linear effects, which importance increases with the reducing of the diffusion term (in the fluid motion equations), due to reduction of viscosity coefficient. The described phenomena of the straightening of the vortex wake and vanishing of the deflected wake region with the Reynolds number requires further experimental investigation.

By the observations of the nature flyers it was found that they operate with the Strouhal number regime of $St_A = 0.2 \div 0.5$, (Taylor, 2003). In the experimental work of (Anderson et al., 1998) it was demonstrated that the highest flapping efficiency occurs for the plunging and pitching profile in the regime of the Strouhal number $St_A = 0.2 \div 0.4$. This regime was called

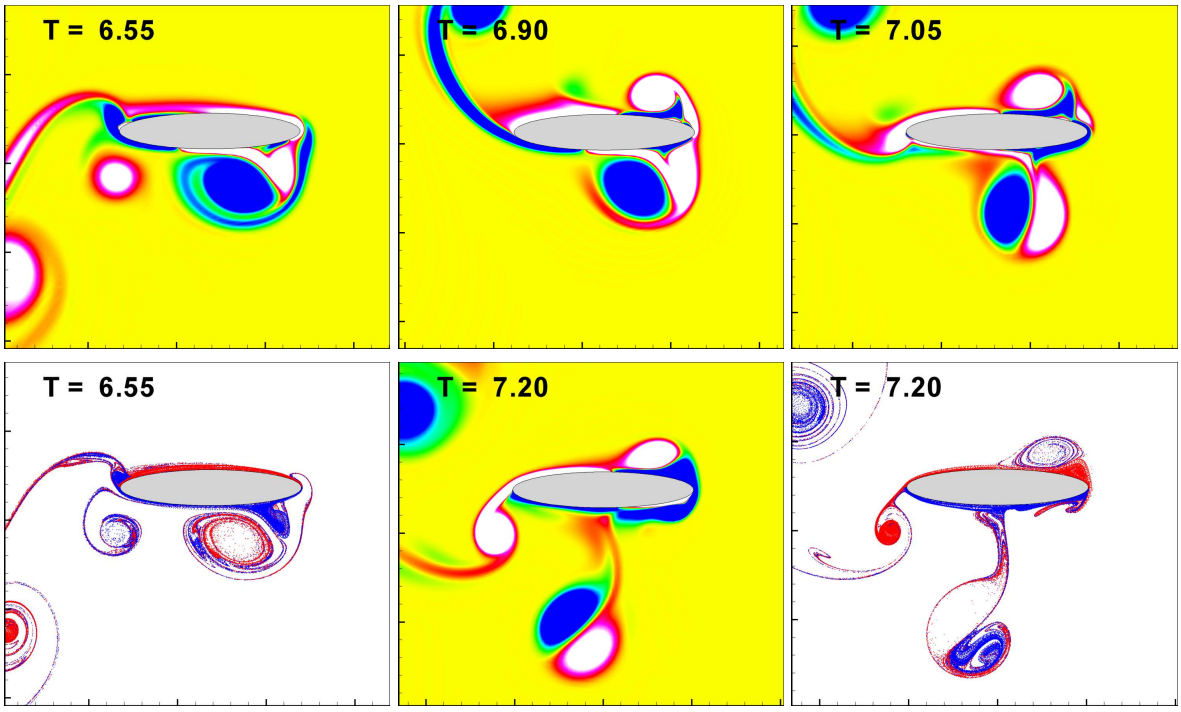

Fig. 13. The boundary eruption phenomena on the flapping area of the profile, $Re = 500$, $St = 0.8$, $A_C = 0.675$. On the figure vortex field is presented for nondimensional time $T = 6.55$ i $T = 7.20$. The visualization with passive markers is also presented.

the optimal Strouhal number regime and the experimental results are in consistence with the observations of the biological locomotion. It's worth to note that from the von Karman analysis of the stability of the vortex position in the wake behind the cylinder (Kochin et al., 1964), the Strouhal number for the stable configuration of the vortex is $St_A = 0.26$. Also the experimental data of the flow over cylinder shown that the Strouhal number for the Karman vortex street is close to the value expressed by Karman in the regime of the Reynolds number $Re = 100 \div 10^4$ which is similar to the regime of the Reynolds number observed for the biological locomotion. In Fig. 9 and 11 the curves of constant Strouhal number St_A was drawn. For simple plunging motion investigated in the present paper, the regime of the Strouhal number connected with the vertical and thrust force production depends on the Reynolds number. For $Re = 100$ the thrust and the vertical force in the range of $St = 0.6 \div 1.1$, that is similar with the results presented for freely moving caused by oscillation profile, (Schnipper et al., 2009). On the other side, the increase of the Reynolds number, the regime with the thrust force production relocate in the diagrams and it encompasses the region with the optimal Strouhal number (St_A) observed in nature.

CONCLUSIONS

The Vortex-In-Cell method was used to model the hydrodynamics effect of the plunging foil. Despite of the 2D fluid flow simplification, the dynamics of fluid motion is very reach and permit to understand the non–linear nature of the flapping effect on the structure of the vorticity flow. The dynamics of the vorticity field is responsible for production of the lift and thrust forces during the flight of the natural flyers and swimmers. We presented the hydrodynamics effect of the simple oscillation of the profile and we found that the vortex wake transitions depends of the Reynolds number. The dynamics of fluid phenomena are related with strong nonlinear dynamics and it's increase with the Reynolds number. The computational result are in qualitative agreement with experimental data although we assumed much smaller Reynolds number and perform the basic plunging motion of the profile.

REFERENCES

Anderson, C. R. and Reider, M. B. (1996). A high order explicit method for the computation of flow about a circular cylinder. *J. Comp. Phys.*, 125.

Anderson, J. M., Streitlien, K., Barret, D. S., and Triantafyllou, M. S. (1998). Oscillating foils of high propulsive efficiency. *J. Fluid. Mech*, 360.

Cottet, G.-H. and Koumoutsakos, P. (2000). *Vorticity Boundary conditions and Related Issues for Finite Difference schemes*. Cambridge University Press, Cambridge.

Godoy-Diana, R., Aider, J.-L., and Wesfreid, J. E. (2008). Transitions in the wake of a flapping foil. *Physical Review E*, 77.

Godoy-Diana, R., Marais, C., Aider, J.-L., and Wesfreid, J. E. (2009). Model for the symmetry breaking of the reverse benard-von karman vortex street produced by flapping foil. *J. Fluid Mech.*, 622.

Gustafson, K. E., Leben, R., and Freymuth, P. (1991). Visualization and computation of hovering mode. *Visualization and computation of hovering mode*.

Jones, K. D., Dohring, C. M., and Platzer, M. F. (1996). Wake structures behind plunging airfoils: A comparison of numerical and experimental results. *AIAA*, 19.

Kochin, N. E., Kibel, I. A., and Rose, N. V. (1964). *Theoretical Hydromechanics*. Wiley-Interscience.

Koumoutsakos, P. and Leonard, A. (1995). High-resolution simulations of flow around an impulsively started cylinder using vortex method. *J. Fluid Mech.*, 296.

Koumoutsakos, P., Leonard, A., and Pepin, F. (1994). Boundary conditions for viscous vortex methods. *J. Comp. Phys.*, 113.

Kudela, H. and Kozlowski, T. (2009). Vortex in cell method for exterior problems. *J. Theor. Appl. Mech.*, 47.

Kudela, H. and Malecha, Z. (2010). Eruption of a boundary layer induced by a 2d vortex patch. *Fluid Dyn. Res.*, 41.

Kudela, H. and Malecha, Z. M. (2009). Viscous flow modelling using the vortex particle method. *Task Quarterly*, 13.

Müller, U. K., Van den Boogaart, J. G. M., and Van Leeuwen, J. L. (2008). Flow patterns of larval fish: undulatory swimming in the intermediate flow regime. *J. Fluids and Struct.*, 211.

Peskin, C. S. and Miller, L. A. (2004). When vortices stick: an aerodynamic transition in tiny insect flight. *J. Exp. Biol.*, 207.

Platzer, M. F. and Jones, K. D. (2000). The unsteady aerodynamics of flapping-foil propellers. *9th International Symposium on Unsteady Aerodynamics Aeroacoustics and Aeroelasticity of Turbomachines Lyon France*.

Ponta, F. L. and Aref, H. (2006). Numerical experiments on vortex shedding from an oscillating cylinder. *J. Fluids and Struct.*, 22.

Sagredo, B. (2003). *Moment conserving Cardinal Splines Interpolation of Compact Support for Arbitrarily Spaced Data*. Research Report No. -10, Zurich Switzerland.

Sane, S. P. (2003). The aerodynamics of insect flight. *J. Exp. Biol.*, 206.

Schnipper, T., Andersen, A., and Bohr, T. (2009). Vortex wakes of a flapping foil. *J. Fluid Mech.*, 633.

Shyy, W., Lian, Y., Tang, J., Viieru, D., and Liu, H. (2008). *Aerodynamics of Low Reynolds Number Flyers*. Cambridge University Press, Cambridge.

Taylor, G. K. (2003). Flying and swimming animals cruise at a strouhal number tuned for high power efficiency. *Nature*, 425.

Thomas, J. W. (1995). *Numerical Partial Differential Equations: Finite Difference Methods*. Springer.

Wang, Z. J. (1999). Efficient implementation of the exact numerical far field boundary condition for poisson equation on an infinite domain. *J. Comp. Phys.*, 153.

Wang, Z. J. (2004). The role of drag in insect hovering. *J. Exp. Biol.*, 207.

Wang, Z. J., Birch, J. M., and Dickinson, M. H. (2000). Unsteady forces and flows in low reynolds number hovering flight: two-dimensional computations vs robotic wing experiments. *J. Exp. Biol.*, 207.

Weinan, E. and Liu, J.-G. (1996). Vorticity boundary conditions and related issues for finite difference schemes. *J. Comp. Phys.*, 66.

Wu, J. C. (1981). Theory for aerodynamics force and moment in viscous flows. *AIAA*, 19.

Wu, J. Z., Ma, H., and Zhou, M. (2005). *Vorticity and Vortex Dynamics*. Springer.